INTERNATIONAL JOURNAL FOR NUMERICAL METHODS IN FLUIDS
Int. J. Numer. Meth. Fluids **29**: 791–810 (1999)

COMPUTATIONS OF RECIRCULATION ZONES OF A CONFINED ANNULAR SWIRLING FLOW

D.L. YOUNG[a,*], C.B. LIAO[b] AND H.J. SHEEN[c]

[a] *Department of Civil Engineering and Hydrotech Research Institute, National Taiwan University, Taipei 10617, Taiwan*
[b] *Graduate Institute of Civil and Hydraulic Engineering, Feng Chia University, Taichung 407, Taiwan*
[c] *Institute of Applied Mechanics, National Taiwan University, Taipei 10617, Taiwan*

SUMMARY

In this paper, a numerical investigation is presented to study the flow structures behind an axially mounted center-body of a confined annular swirling flow. Based on the transient, axisymmetric Navier–Stokes equations, the projection method is used to solve the pressure Poisson equation to retain the equation of continuity. The velocity is then solved by using the explicit Adams–Bashforth scheme. By this numerical algorithm, second-order accuracy in both time and space discretizations can be obtained. Discussions on the computational length and computing efficiency are made. For the annular swirling flow, the characteristics of the flow structures are dependent on two dimensionless parameters, the Reynolds number *Re*, and the swirl number *S*. Several flow patterns can be obtained by this numerical simulation. The lengths of the recirculation zone in various flow conditions are also calculated. It is found that the higher the swirl number, the more complex and unstable the flow. The present computational results are in reasonable agreement with those of the experiment obtained by LDA measurements and smoke visualization. Copyright © 1999 John Wiley & Sons, Ltd.

KEY WORDS: annular swirling flow; projection method; recirculation zone; flow pattern; Reynolds number; swirl number

1. INTRODUCTION

A swirling flow is a flow with spiral motion in the tangential direction in addition to the axial and radial directions. The use of a swirling flow from a swirl generator in a combustion chamber can improve the flame stability by the formation of a toroidal recirculation zone (Beer and Chigier [1]). The flame length can be reduced and the size of the combustion chamber can be minimized. Moreover, the introduction of swirling motion to a jet flow can lead to a higher ambient entrainment flow and enhance flow mixing. Many researchers have conducted relative studies on the aerodynamic properties of swirling flow, e.g. Syred and Beer [2] and Lilley [3].

For the effects of the center-body geometry on the flow structures, Taylor and Whitelaw [4] studied the velocity characteristics behind various axisymmetric bluff bodies. They concluded that the recirculation bubble was shorter and narrower for a flow with a 45° cone than with a disk, and that a decrease of the blockage ratio would lengthen and narrow the recirculating bubble. The effects of the blockage ratio were also investigated. Li and Tankin [5] carried out

---

* Correspondence to: Department of Civil Engineering and Hydrotech Research Institute, National Taiwan University, Taipei 10617, Taiwan. Tel.: +886 2 23626114; fax: +886 2 23639258; E-mail: dlyoung@hy.ntu.edu.tw

CCC 0271–2091/99/070791–20$17.50

Received December 1997
Revised March 1998

an experiment for isothermal and combusting flows with various axially aligned cylindrical bluff bodies at the exit of an annular jet by a flow visualization technique. The variations of recirculation length in the near-wake region behind the bluff body were discussed, and the asymptotic solutions for the recirculation length were also derived. In general, the recirculating length changed with the flow conditions and also the geometries of the bluff body.

Chigier and Beer [6] made measurements in an unconfined swirling annular jet, where the degree of swirl was varied by various proportions of air introduced axially and tangentially into the swirl generator. They concluded that a closed toroidal vortex was formed behind the central bluff body due to the comparatively large subatmospheric pressure in the near-wake region at sufficiently high degrees of swirl. Further, the strength and size of this vortex increased as the swirl strength increased.

Regarding the effects of a confined boundary, Rhode *et al.* [7] investigated an annular swirling jet with various swirling vane angles and different side-wall expansion angles. They found that increasing the swirling vane angle provoked the existence of a central recirculation bubble, and that this zone length was only slightly affected by the side-wall expansion angle.

For the formation of a central recirculation zone behind a center-body in weak and intermediate swirl conditions, Escudier and Keller [8] mentioned that as the swirl strength was increased, the axial–radial flow field did not change significantly until a certain critical swirl was reached, and then an isolated axisymmetric recirculation zone appeared in the downstream region. As the degree of swirl was further increased, the recirculation zone moved upstream. The so-called isolated recirculation zone meant the location of vortex breakdown, which is a vortex flow with abrupt and drastic changes in the axial velocity component. The characteristics of vortex breakdown are commonly recognized as the formation of a stagnation point on the axis and a sudden widening of the vortex core due to a region of reversed axial flow. Some observations of the vortex breakdown phenomenon were presented by Harvey [9] and Sarpkaya [10]. Shtern *et al.* [11] conducted theoretical studies and simulations on the vortex breakdown phenomenon and gave several examples of applications based on an analytical solution of the Navier–Stokes equations.

The parameter to characterize the swirl strength of a swirling flow is a very important consideration. Sheen *et al.* [12] made an experimental investigation by using a radial-type swirl generator, and concluded that the swirl number was dependent on the vane angle as well as the Reynolds number, especially in the laminar flow regime. A correlation for the swirl number with various Reynolds numbers was derived.

Concerning the effects of the axially aligned center-body on the flow structure of a confined annular flow, Sheen *et al.* [13] carried out an experiment for a non-swirling annular flow over an axisymmetric sudden expansion. Four different flow patterns were observed under various Reynolds number conditions. Bifurcation of flow structure in the processes as the Reynolds number was either increased or decreased was also reported.

The characteristics of the recirculation zone behind the center-body for an annular swirling flow were experimentally investigated by Sheen *et al.* [14] with visual observation and LDA measurement techniques. By using the parameters of the swirl number S, and the Reynolds number Re, seven different flow patterns were classified. They were open-top toroid, closed toroid, vortex-shedding, shear layer shedding, transition, prepenetration, penetration, vortex breakdown and attachment. Characteristics of the flow modes in (S, Re) domain were thoroughly investigated. A unified analytical expression was derived for the recirculation lengths in all flow conditions and the predictions were in reasonable agreement with the experimental results.

In this paper, a numerical scheme for incompressible axisymmetric flow is proposed to simulate the flow structures of a confined annular swirling flow. The geometry of the flow field, the testing flow conditions and the inflow boundary conditions are adopted from the experiment of Sheen *et al.* [14]. A second-order-accurate finite difference method is applied to solve the axisymmetric Navier–Stokes equations. Several numerical simulations are carried out to investigate various flow conditions, including both the non-swirling flow ($S=0$) and the swirling flow ($S>0$) in the laminar flow regime. Comparisons of the computational results with the experimental data are also made.

Since the present numerical scheme is based on the assumption of axisymmetry, the simulations will be restricted to axisymmetric cases of the swirling flows. Consequently, such three-dimensional flow patterns as vortex shedding, open-top toroid, transition, etc. observed experimentally by Sheen *et al.* [14] could not be predicted by this numerical scheme. A further simulation model based on a three-dimensional numerical scheme is needed to obtain 3D flow structures.

2. FORMULATIONS OF THE PROBLEM

The basis of the present study is the experiments conducted by Sheen *et al.* [14] with the test set-up as shown in Figure 1. The air stream passed through a settling chamber into a 16-guide-vane swirl generator. The swirling airflow was then sent to the test section through an annulus. The annular airflow pipe had an inner diameter d_i of 21.7 mm and an outer diameter d_o of 45.3 mm. The confined boundary was a sudden expansion plexiglass tube with an inner diameter D_e of 130 mm, which was placed at the exit of the annular pipe. The length of the confined tube used in the experiment was 1.2 m. The computational domain is also shown in Figure 1. The computational length L in the axial direction for numerical simulation is chosen to be shorter than that of the experiment in order to reduce the computing time. Several computational lengths are also used in this study for computing efficiency.

2.1. Governing equations

The governing equations, including the continuity equation and the Navier–Stokes equations, in cylindrical co-ordinates for an axisymmetric, incompressible, swirling flow can be expressed in dimensionless form as

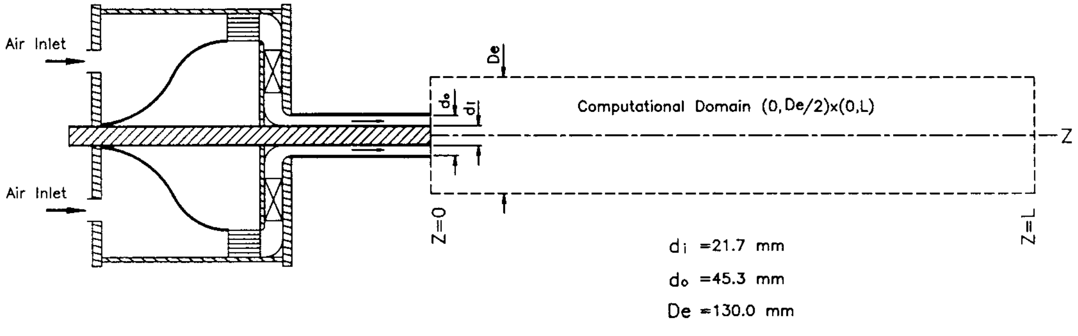

Figure 1. Schematic diagram of the radial-type swirl generator (Sheen *et al.* [14]), the test section, and the computational domain.

$$\frac{1}{r}\frac{\partial}{\partial r}(ru)+\frac{\partial w}{\partial z}=0, \tag{1}$$

$$\frac{\partial u}{\partial t}+u\frac{\partial u}{\partial r}+w\frac{\partial u}{\partial z}-\frac{v^2}{r}+\frac{\partial p}{\partial r}-\frac{1}{Re}\left(\nabla^2 u-\frac{u}{r^2}\right)=0, \tag{2}$$

$$\frac{\partial v}{\partial t}+u\frac{\partial v}{\partial r}+w\frac{\partial v}{\partial z}+\frac{uv}{r}-\frac{1}{Re}\left(\nabla^2 v-\frac{v}{r^2}\right)=0, \tag{3}$$

$$\frac{\partial w}{\partial t}+u\frac{\partial w}{\partial r}+w\frac{\partial w}{\partial z}+\frac{\partial p}{\partial z}-\frac{1}{Re}\nabla^2 w=0, \tag{4}$$

where r is the radial, θ is the azimuthal, z is the axial co-ordinate, u, v, w are the velocities in r-, θ-, z-components respectively, t is time, p is the dynamic pressure and

$$\nabla^2=\frac{1}{r}\frac{\partial}{\partial r}\left(r\frac{\partial}{\partial r}\right)+\frac{\partial^2}{\partial z^2}$$

is the axisymmetric Laplacian operator. The Reynolds number is defined by $Re=\bar{w}(d_o-d_i)/v$, where $\bar{w}$ is the volumetric average axial velocity of the inflow, and v is the kinematic viscosity of the air. The variables are non-dimensionalized by using the hydraulic diameter of the annulus, $d_h=d_o-d_i$, the mean axial velocity, $\bar{w}$, and the pressure coefficient, $\rho\bar{w}^2$.

2.2. Boundary conditions

The inlet velocity profiles, which include the axial, radial and azimuthal components, are based on the experimental data of Sheen *et al.* [14]. These results were obtained from LDA measurements. It was found that the swirl strength was strongly dependent on the Reynolds number as well as on the guide-vane angle under low Reynolds number conditions. At the symmetric axis, zero radial and azimuthal velocity and zero-gradient condition for the axial velocity are imposed. No-slip boundary conditions are applied for the confined wall boundary. At the outlet of the test section, the axial velocity can be determined from the overall mass conservation and the linearized convective outflow boundary condition [15]. The boundary conditions are listed as follows:

(i) Inflow boundary condition

$$u,\ v,\ w \text{ are given} \quad \text{on} \quad z=0, \quad 0\le r\le D_e/2d_h. \tag{5}$$

(ii) Symmetric boundary condition on the center axis

$$u=v=\frac{\partial w}{\partial r}=0 \quad \text{on} \quad r=0, \quad 0\le z\le L/d_h. \tag{6}$$

(iii) No-slip boundary condition on the confined pipe wall

$$u=v=w=0 \quad \text{on} \quad r=D_e/2d_h, \quad 0\le z\le L/d_h. \tag{7}$$

(iv) Outflow boundary condition

$$\frac{\partial w}{\partial t}+\bar{w}\frac{\partial w}{\partial z}=0 \quad \text{on} \quad z=L/d_h, \tag{8}$$

where L is the computational length in the axial direction. Figure 2 gives the schematic diagram of the flow field in cylindrical co-ordinates and the corresponding boundary conditions.

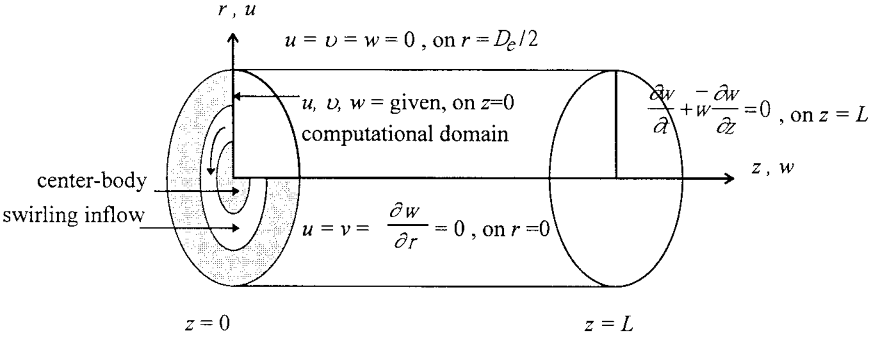

Figure 2. Schematic diagram of the flow field in cylindrical co-ordinates and the corresponding boundary conditions.

2.3. Numerical scheme

The primitive variables (u, v, w, p) formulation is used to solve the governing Navier–Stokes equations. The marker and cell (MAC) staggered computational grid system [16] is adopted to discretize the partial differential equations. The projection method is applied to obtain the pressure Poisson equation such that the equation of continuity can be satisfied automatically [17]. The velocities are then solved by an explicit Adams–Bashforth scheme with central differencing in spatial discretization. Therefore, a second-order-accurate numerical solution in both time and space calculation can be obtained.

2.3.1. Explicit Adams–Bashforth scheme for velocities. From Equations (2)–(4) and using the explicit Adams–Bashforth scheme, the discretized momentum equations can be derived as

$$\frac{u^{n+1}-u^{n}}{\Delta t}+f^{n}+\frac{\delta r}{\Delta r}p^{n+1}=0, \tag{9}$$

$$\frac{v^{n+1}-v^{n}}{\Delta t}+g^{n}=0, \tag{10}$$

$$\frac{w^{n+1}-w^{n}}{\Delta t}+h^{n}+\frac{\delta z}{\Delta z}p^{n+1}=0, \tag{11}$$

where

$$f^{n}=\frac{3}{2}A^{n}-\frac{1}{2}A^{n-1}, \qquad g^{n}=\frac{3}{2}B^{n}-\frac{1}{2}B^{n-1}, \qquad h^{n}=\frac{3}{2}C^{n}-\frac{1}{2}C^{n-1},$$

and

$$A=u\frac{\delta r}{\Delta r}u+w\frac{\delta z}{\Delta z}u-\frac{v^{2}}{r}-\frac{1}{Re}\left(L^{2}u-\frac{u}{r^{2}}\right),$$

$$B=u\frac{\delta r}{\Delta r}v+w\frac{\delta z}{\Delta z}v+\frac{uv}{r}-\frac{1}{Re}\left(L^{2}v-\frac{v}{r^{2}}\right),$$

$$C=u\frac{\delta r}{\Delta r}w+w\frac{\delta z}{\Delta z}w-\frac{1}{Re}L^{2}w$$

$$L^{2}=\frac{1}{r}\frac{\delta r}{\Delta r}\left(r\frac{\delta r}{\Delta r}\right)+\frac{\delta_{z}^{2}}{\Delta z^{2}},$$

where δr, δz, δ_z^2 are the differencing operators, $\delta r(f_{i,j}) = f_{i+1/2,j} - f_{i-1/2,j}$ and $\delta z(f_{i,j}) = f_{i,j+1/2} - f_{i,j-1/2}$ are the first derivatives, $\delta_z^2(f_{i,j}) = f_{i,j+1} - 2f_{i,j} + f_{i,j-1}$ is the second derivative based on the central difference scheme, and Δr, Δz are the grid sizes in the r-, z-directions. The MAC staggered grid system, as depicted in Figure 3, is used in the numerical computation.

2.3.2. Projection method for pressure. Taking divergence to Equations (9) and (11), one can obtain the pressure Poisson equation

$$\left[\frac{1}{r}\frac{\delta r}{\Delta r}\left(r\frac{\delta r}{\Delta r}\right) + \frac{\delta_z^2}{\Delta z^2}\right]p^{n+1} = \frac{1}{r}\frac{\delta r}{\Delta r}\left[r\left(\frac{u^n}{\Delta t} - f^n\right)\right] + \frac{\delta z}{\Delta z}\left(\frac{w^n}{\Delta t} - h^n\right) \tag{12}$$

with the Neumann boundary conditions as follows:

$$\frac{\delta r}{\Delta r}p^{n+1} = -\left(\frac{u^{n+1} - u^n}{\Delta t} + f^n\right) \quad \text{on} \quad r = 0, \quad D_e/2d_h, \tag{13}$$

$$\frac{\delta z}{\Delta z}p^{n+1} = -\left(\frac{w^{n+1} - w^n}{\Delta t} + h^n\right) \quad \text{on} \quad z = 0, \quad L/d_h. \tag{14}$$

The continuity equation (1) is thereby satisfied when the pressure p^{n+1} is solved from the above Poisson equation (12) with the Neumann boundary conditions (13) and (14). There is only one unknown on the boundary condition (14), namely w^{n+1} on the outflow boundary $z = L/d_h$. An iteration procedure is applied to solve the pressure and velocity fields until the pressure and velocity converge in each time step [18]. An innovative method to solve the outflow velocity w^{n+1} is applied in this study, which is called the linearized convective outflow boundary condition. Using this method, the flow properties, which transports downstream to the pipe exit plane by the average velocity $\bar{w}$, are taken into consideration. The outflow velocity w^{n+1} can then be calculated from (8).

Another advantage of using this outflow boundary condition is that the length of the computational domain in the axial direction can be reduced significantly. Therefore, the computing efficiency is increased considerably. The effects of the length for the computational domain will be discussed later.

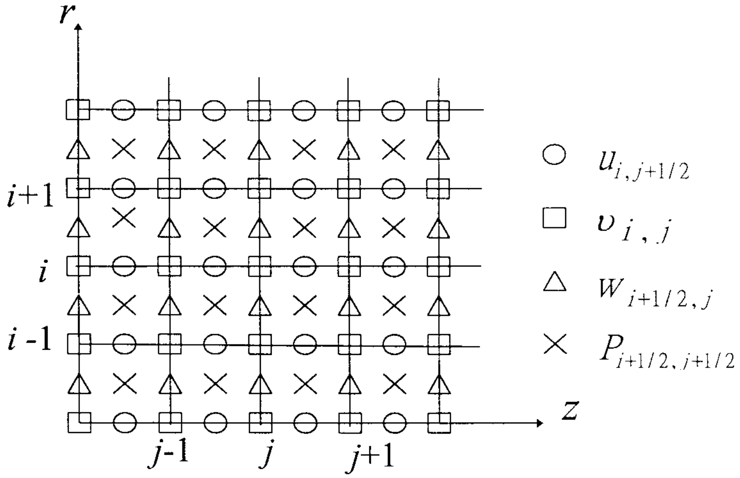

Figure 3. The MAC staggered grid system for the numerical model.

When the velocity w^{n+1} on the outflow boundary is obtained, the pressure field p^{n+1} can be solved from Equations (12)–(14). Direct computation, based on the fast Fourier transform (FFT) and a tridiagonal matrix algorithm (TDMA), is employed to obtain p^{n+1} instead of using the iteration method, e.g. successive over relaxation (SOR) method. The following gives a detailed description for this algorithm.

The discretized differencing equation (12) in the z-direction at $j = 1/2$ point (first grid point in the z-direction, see Figure 3) can be written as

$$\cdots + \frac{1}{\Delta z}\left(\frac{\delta_z}{\Delta z} p^{n+1}_{i+1/2,1} - \frac{\delta_z}{\Delta z} p^{n+1}_{i+1/2,0}\right) = \cdots + \frac{1}{\Delta z}\left(\left(\frac{w^n}{\Delta t} - h^n\right)_{i+1/2,1} - \left(\frac{w^n}{\Delta t} - h^n\right)_{i+1/2,0}\right). \tag{15}$$

From (14), we have

$$\frac{\delta_z}{\Delta z} p^{n+1}_{i+1/2,0} = -\left(\frac{w^{n+1} - w^n}{\Delta t} + h^n\right)_{i+1/2,0}. \tag{16}$$

From (15) and (16), we can let $h^n = 0$ and $(\delta_z/\Delta z)p = 0$ on the boundary $z = 0$. The remaining three boundary conditions in (13) and (14) can be processed by using the same argument. If we let $f^n = 0$ on $r = 0$ and $r = D_e/2d_h$; $h^n = 0$ on $z = 0$ and L/d_h, then the pressure Poisson equation and the boundary conditions can be rewritten as

$$\left[\frac{1}{r}\frac{\delta r}{\Delta r}\left(r\frac{\delta r}{\Delta r}\right) + \frac{\delta z^2}{\Delta z^2}\right] p^{n+1} = R^n, \tag{17}$$

$$\frac{\delta r}{\Delta r} p^{n+1} = 0 \quad \text{on} \quad r = 0, \quad D_e/2d_h, \tag{18}$$

$$\frac{\delta z}{\Delta z} p^{n+1} = 0 \quad \text{on} \quad z = 0, \quad L/d_h \tag{19}$$

Hence p^{n+1} can be solved from Equations (17)–(19) by using the FFT and a TDMA. Let

$$p^{n+1}_{i+1/2,j+1/2}(r, z) = \sum_{k=0}^{N-1} a_k(r) \cos k\pi z_{j+1/2}, \quad j = 0, 1, 2, \ldots, N-1, \tag{20}$$

then the pressure p^{n+1} will satisfy the boundary conditions (19).

For (17), R^n is expanded by using Fourier cosine series

$$R^n_{i+1/2,j+1/2}(r, z) = \sum_{k=0}^{N-1} b_k(r) \cos k\pi z_{j+1/2}, \quad j = 0, 1, 2, \ldots, N-1. \tag{21}$$

Substituting Equations (20) and (21) into (17), we have

$$\left[\frac{1}{r}\frac{\delta r}{\Delta r}\left(r\frac{\delta r}{\Delta r}\right) - \frac{4\sin^2\dfrac{k\pi\Delta z}{2}}{\Delta z^2}\right] a_k(r) = b_k(r), \quad k = 0, 1, \ldots, N-1, \tag{22}$$

$$\frac{\delta r}{\Delta r} a_k(r) = 0 \quad \text{on} \quad r = 0, \quad D_e/2d_h. \tag{23}$$

In brief, the numerical procedures for solving the pressure field are summarized as follows (Young and Liao [19])

(i) solve $b_k(r)$ from (21) by using the FFT,

(ii) from (22) and (23), $a_k(r)$ can be calculated, which is a tridiagonal matrix system, and can be easily solved by the conventional equation solver,

(iii) the pressure p^{n+1} is obtained from (20) by using the inverse FFT.

3. RESULTS AND DISCUSSION

As mentioned in Sheen *et al.* [14], the controlled parameters for the flow structure of a confined annular swirling flow included the Reynolds number *Re*, and the swirl number *S*. The swirl strength was adjusted mainly by varying the vane angle ϕ of the guide-vane cascade in the radial-type swirler (see Figure 1). The swirl number *S* is defined to be the ratio of the axial flux of angular momentum to the axial flux of axial momentum, as was originally proposed by Chigier and Beer [6]

$$S = \frac{\displaystyle\int_0^R wvr^2 \, \mathrm{d}r}{R \displaystyle\int_0^R w^2 r \, \mathrm{d}r}. \tag{24}$$

Based on the experimental results, Sheen *et al.* [12] further proposed a correlation for the swirl number *S* for the annular swirling flow given as

$$S = 0.75 \frac{\bar{v}}{\bar{w}}, \tag{25}$$

since the swirl number *S* was linearly proportional to the ratio of volumetric mean azimuthal to axial velocity, where $\bar{v}$ is the volumetric azimuthal velocity at the annulus exit. In this study, the results of numerical simulation are in good agreement by using either (24) or (25).

3.1. Model verification

Second-order accuracy in both time and space discretization can be obtained by using the proposed numerical scheme as mentioned before. Furthermore, the time-dependent transient solution can be solved by this scheme. As far as the steady state solution is concerned, numerical computations can be executed until the whole field reaches a steady state.

In order to compare the numerical solutions with the experimental results, only the steady state solutions are used for model verification. A uniform grid system is used in this study since the FFT algorithm is applied. This computation employs 128×256 grid points for the flow field study. In this simulation, the confined pipe diameter D_e is 130 mm, the computational pipe length L is chosen to be 226.5 mm, $\Delta r = 0.02$, $\Delta z = 0.04$, and the time step $\Delta t = 0.01$. Since the computational length L is very short, which is only about $5d_o$, and if the initial condition of the whole field is set as motionless fluid, the calculation will diverge for higher Reynolds number conditions, e.g. $Re \geq 600$. Under this circumstance, the computational length L should be increased. This leads to a considerable increase in the computer memory and computing time. However, the above mentioned problem can be improved by employing the following method so that the steady state solutions can be obtained for the flow with the Reynolds number as high as 1900.

The computation is started with motionless fluid in the whole fields initially and with $Re = 100$ and $S = 0$. As the steady state solution is reached, the Reynolds number is then increased to $Re = 200$ and the same computation is repeated. Steady state condition is

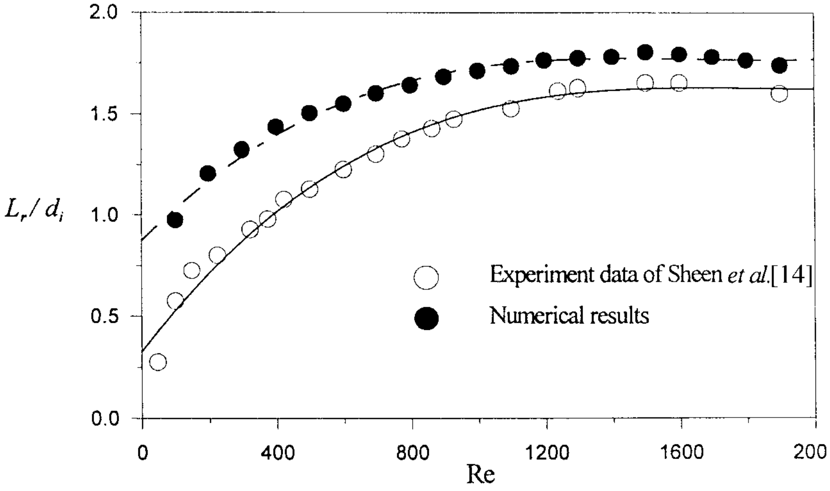

Figure 4. Relationship between the length of the central recirculation bubble behind the center-body and the Reynolds number, *Re*.

considered to be reached when the root mean square residues of the accelerations, $\partial u/\partial t$, $\partial v/\partial t$ and $\partial w/\partial t$, are less than 10^{-4}. The increment of the Reynolds number for each computation is 100. For the swirling flow cases, the swirl number S is set to 0 initially. The increment of the swirl number for each computation is about 0.05. By this numerical procedure, the flow simulation can be executed to as high as $Re = 1900$. For the non-swirling flow, the computational results for the relationship between the recirculation length L_r behind the center-body and the Reynolds number *Re* is shown in Figure 4. It is found that the trend of the computational results is in general agreement with the experimental data. The values of the calculated results deviate from the experiment results when the Reynolds number is low. However, as the Reynolds number is increased, the solutions are in better agreement with the experiment data.

Comparisons of the flow pattern between the numerical and the experimental results for both the non-swirling and the swirling flow conditions are made for $Re = 1265$. Figure 5 gives the steady state streamlines for $Re = 1265$ and $S = 0$. Under this flow condition, the flow

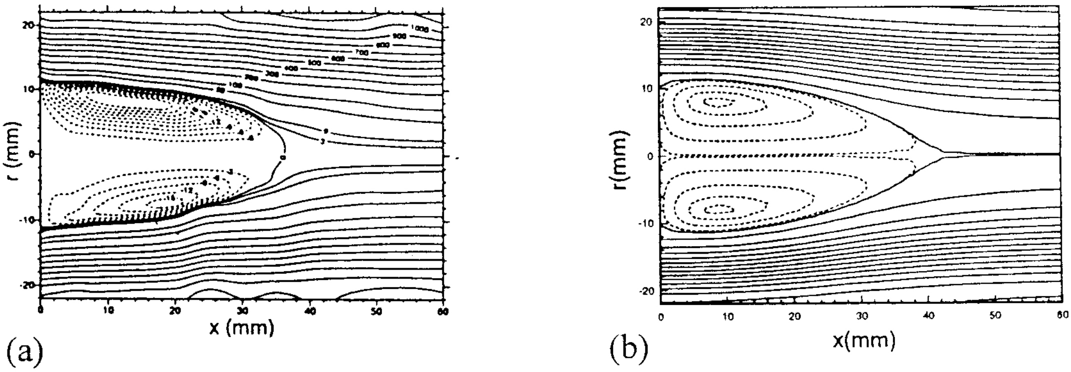

Figure 5. Comparison of the steady state streamlines for $Re = 1265$ and $S = 0$; (a) experimental data of Sheen *et al.* [14], (b) computational results.

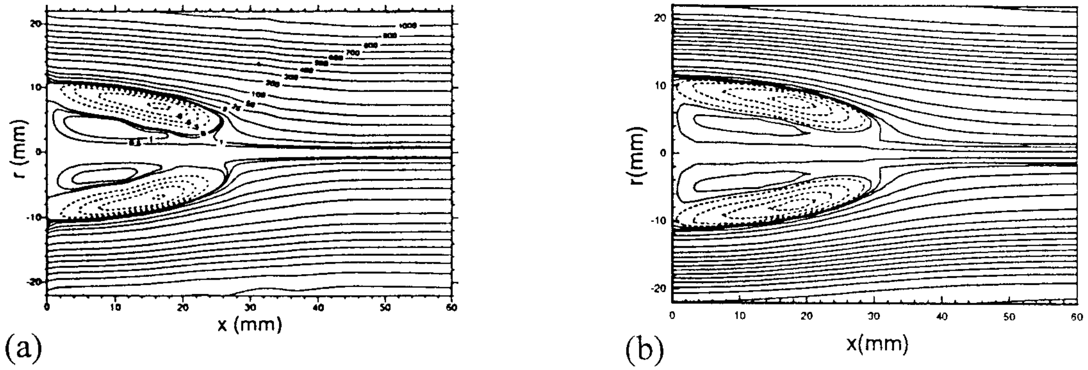

Figure 6. Comparison of the steady state streamlines for $Re = 1265$ and $S = 0.12$; (a) experimental data of Sheen *et al.* [14], (b) computational results.

pattern was called vortex-shedding flow regime by Sheen *et al.* [14]. Physically, this flow is asymmetric and unsteady in nature, vortex-shedding from the central recirculation bubble was observed. The vorticity is shed from the annular vortex behind the center-body, in such a form as a succession of distorted vortex loops that are not symmetric about the central axis. The free separation surface of the central recirculation bubble is thus quite unstable. In Figure 5(a), the time mean averaged streamlines for the experimental results are depicted. For the steady state solutions, only a toroidal recirculation bubble behind the center-body is obtained, as shown in Figure 5(b).

For the annular swirling flow cases, the inflow boundary conditions (5) are changed with the addition of the azimuthal velocity component v. Figure 6 illustrates the results from the experiments and the steady state streamlines from the computations for $Re = 1265$ and $S = 0.12$. This flow pattern was called the penetration by Sheen *et al.* [14]. In this flow regime, an annular vortex and an inverted triangular zone both exist in the recirculation zone. As the swirling flow has an effect of stabilizing the central recirculation zone, the free separation surface of the recirculation bubble becomes more stable for a swirling flow than that of a non-swirling flow. The computational results are in better agreement with the experimental data than in the non-swirling case.

For the higher swirl number conditions, an isolated recirculation zone (or the so-called vortex breakdown) can be obtained downstream the central recirculation bubble. Figure 7 gives the steady state solutions of the u–w vectors and the streamlines for $Re = 1265$ and $S = 0.23$. Sheen *et al.* [14] referred to this flow regime as vortex breakdown. The axial velocities near the recirculation bubble are in a jet-like form. While near the vortex breakdown, the axial velocity profiles become wake-like. The computational results are in agreement with the experimental ones. The recirculation length L_r decreases as the swirl number is increased. Moreover, the location of the vortex breakdown region moves upstream as the swirl strength is increased.

Further, as the swirl number is increased to a critical value, the isolated recirculation zone finally attaches to the apex of the central recirculation bubble behind the center-body. This flow regime was called attachment and the critical values of the swirl number can be found in Sheen *et al.* [14]. The flow structure for the attachment regime becomes very unstable. Since the flow structure becomes very complex and unstable, under some flow conditions, the steady state solution could not be obtained and much longer computing time is needed to have a steady state solution even if it exists.

(a) streamlines (c) streamlines

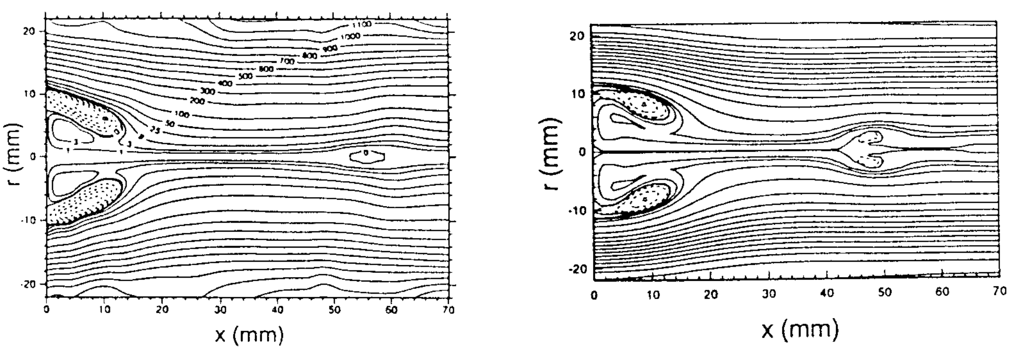

(b) velocity vectors (d) velocity vectors

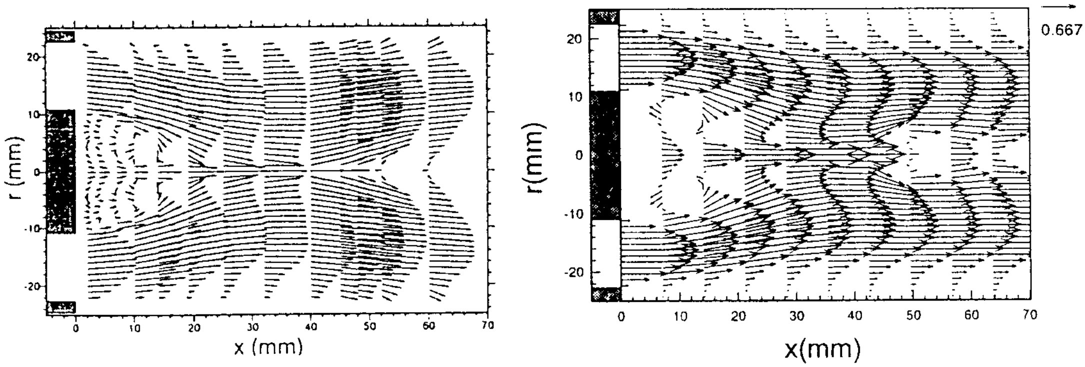

Figure 7. Comparison of the steady state $\boldsymbol{u}$–$\boldsymbol{w}$ vectors and the streamlines for $Re = 1265$ and $S = 0.23$; (a), (b) experimental data of Sheen *et al.* [14]; (c), (d) computational results.

3.2. Transient solution of flow for Re = 300

To investigate the transient phenomena of the flow structure for the lower Reynolds number conditions, computations of two cases are carried out. One is a non-swirling flow with $Re = 300$, $S = 0$, and the other one is a swirling flow with $Re = 300$, $S = 0.3$. In order to observe the developing processes of the inflow, the computational length L is increased to 543.6 mm, or $L = 12\ d_o$. A 128×384 grid system is used and $\Delta r = 0.02$, $\Delta z = 0.06$, the time step $\Delta t = 0.01$, and with motionless fluid initially.

A series of time evolution flow structure with the computed streamlines for the case of $Re = 300$ and $S = 0$ is shown in Figure 8. At the initial time step, a central recirculation bubble behind the center-body and a vortex ring behind the sudden expansion can be observed simultaneously near the inflow plane. The vortex ring moves downstream as time is increased and can be regarded as the flow front. A second vortex ring near the corner region is induced as the original vortex moves downstream. As time is increased, both vortices are stretched in the axial direction. When the flow front passes through the outflow boundary, the whole field develops gradually to steady state when $t = 121.36$. During the developing period, a weak corner vortex can be observed behind the expansion step. The corner vortex finally disappears

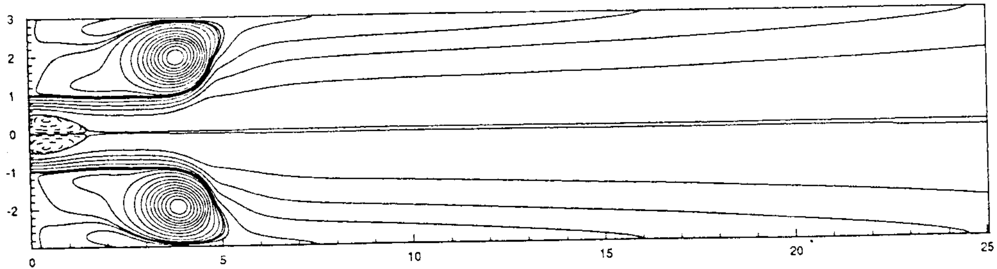

(a) t=10.76

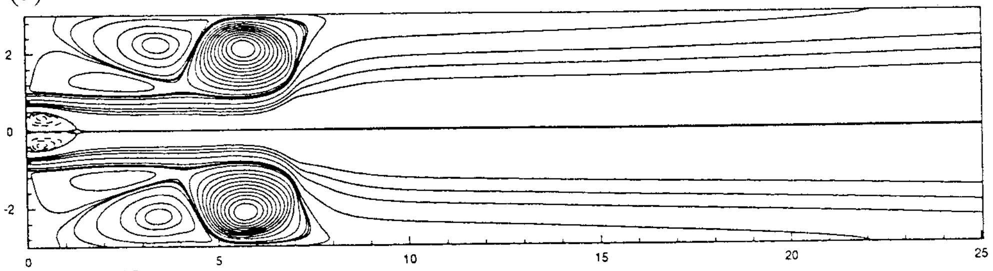

(b) t=21.52

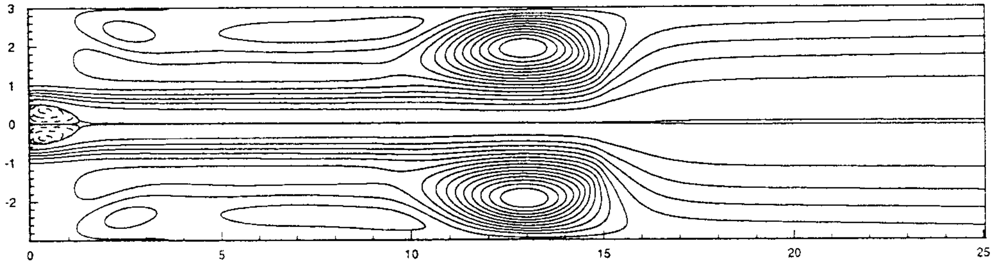

(c) t=43.04

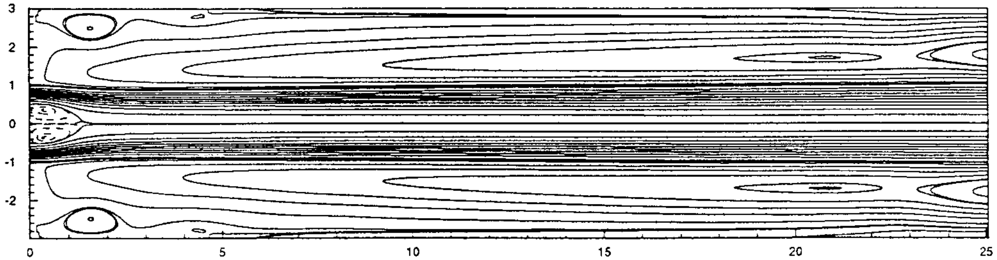

(d) t=75.32

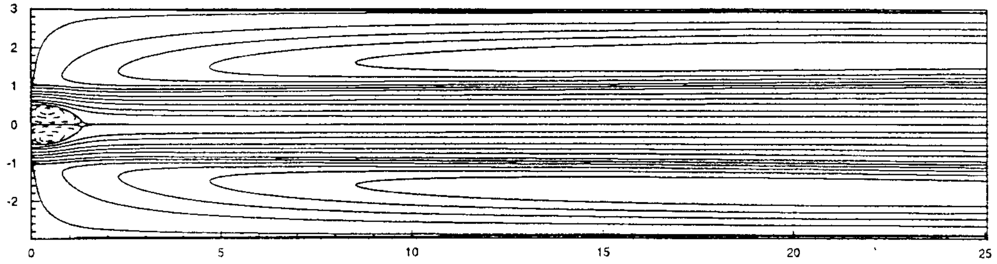

(e) t=121.36

Figure 8. The transient solutions of the streamlines for $Re = 300$ and $S = 0$.

when the flow reaches a steady state. However, the size of the central recirculation zone remains almost constant during this transient period. Further, since the central recirculation bubble is small in size, with an order of the diameter of the center-body d_i, the corner recirculation length is comparatively large, as was mentioned by Sheen *et al.* [14].

Figure 9 shows the transient solutions for a swirling flow condition with $Re = 300$ and $S = 0.3$. As seen in this figure, the transient process of the flow structure of a swirling flow is quite different from that of a non-swirling case and becomes much more complicated and unstable. At the initial time step, the central recirculation bubble is much larger than that in a non-swirling flow. Further, the size of the central recirculation bubble is increased as time is increased. Similar to the last case, a vortex ring around the central recirculation bubble is also formed initially. This annular vortex moves downstream as time is increased. However, the propagation speed of this vortex is slower than in a non-swirling case. The central recirculation bubble grows and stretches in the axial direction as time is further increased. As the steady state is reached, the central recirculation zone becomes much larger than in other flow regimes. The steady state solution is obtained until $t = 497.85$, about four times longer than in the non-swirling flow case. The flow pattern of this flow condition is attachment as mentioned in the last section. For this flow regime, the isolated recirculation zone (vortex breakdown) joins the central recirculation bubble to form a large central recirculation zone that leads to a small corner recirculation zone behind the sudden expansion. The flow regime of attachment, for the flow condition of $Re = 300$ and $S = 0.3$, obtained by this numerical model is different from that observed experimentally. The reason for this discrepancy may be attributed to the different physical conditions in the simulation and the experiment, such as velocity fluctuations, inlet velocities and flow disturbances, etc.

Figure 10(a) depicts the time history for the root mean square values of the acceleration $\partial w/\partial t$ for the last two cases, $Re = 300$ and $S = 0$; $Re = 300$ and $S = 0.3$. The local velocity w at the location of $(0.75, 3.13)$ for both cases is shown in Figure 10(b). For the non-swirling case, the solutions can converge to steady state in shorter time than the swirling flow case. Moreover, the flow structure in the swirling flow is more complex and unstable than in the non-swirl case as can be seen in this figure.

3.3. The influence of computational length

For the effects of the computational length on the numerical results, Figure 11 gives the results of the steady state streamlines for a non-swirling flow case, $Re = 630$ and $S = 0$. Two computational lengths are chosen for the numerical simulation, $L = 6d_o$ and $L = 12d_o$. With the same mesh size, as the computational length is increased twice, the grid points are accordingly increased from 128×256 to 128×512. Therefore, the computational time and the required memory will be doubled. As shown in this figure, the results from both calculations are nearly the same for the whole flow field. The use of the outflow boundary condition in this numerical simulation has a significant effect on reducing the required computational length and leads to an increase in computing efficiency. Similar results are also obtained for the simulations of other flow cases.

3.4. The influence of swirl number

The effects of the swirl number on the confined annular flow are investigated for the case of $Re = 630$ with the swirl number S ranging from 0 to 0.25. Under these flow conditions, the flow regimes will include vortex shedding, transition, prepenetration, penetration, and vortex breakdown as indicated by Sheen *et al.* [14]. The introduction of swirling motion into the

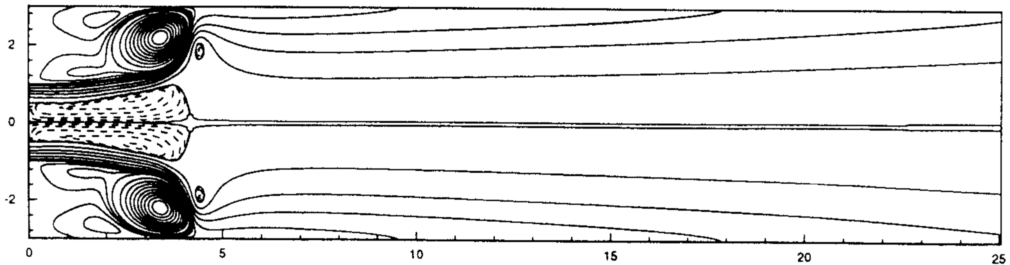

(a) $t=10.76$

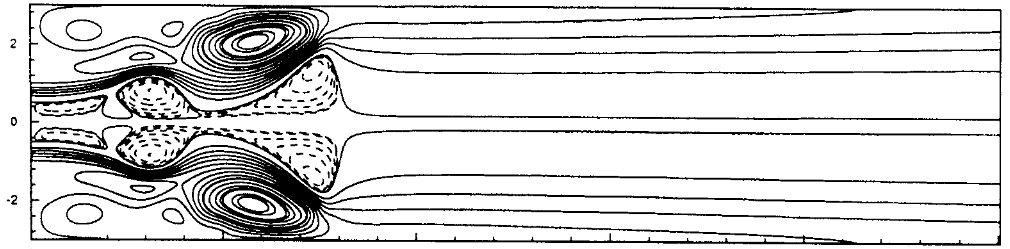

(b) $t=32.28$

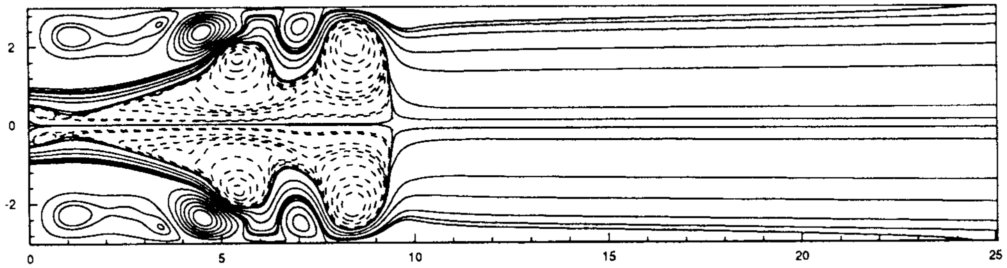

(c) $t=43.04$

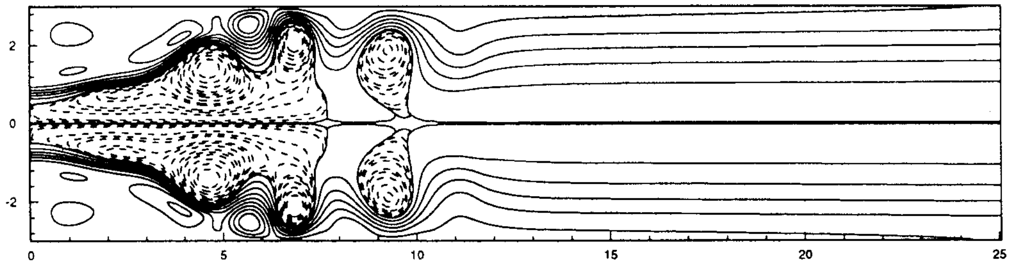

(d) $t=53.80$

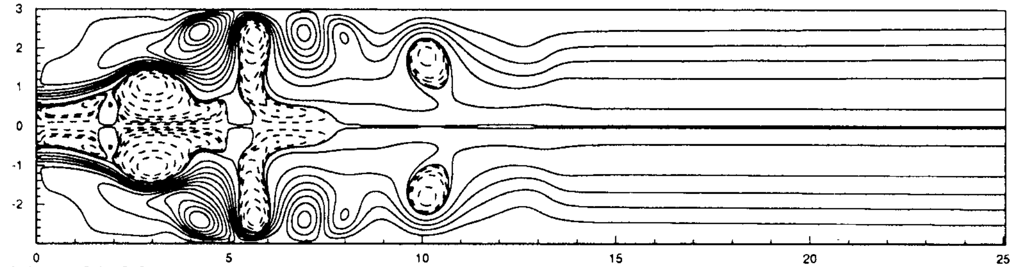

(e) $t=64.56$

Figure 9. The transient solutions of the streamlines for $Re = 300$ and $S = 0.3$.

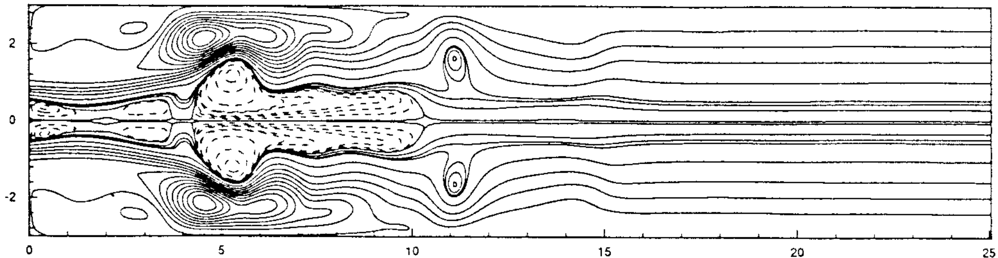

(f) t=75.32

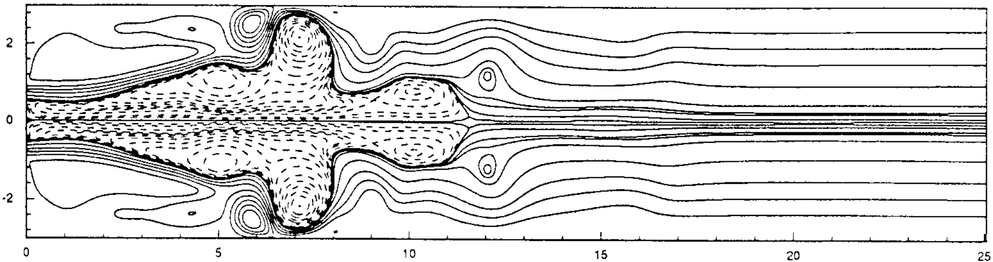

(g) t=86.08

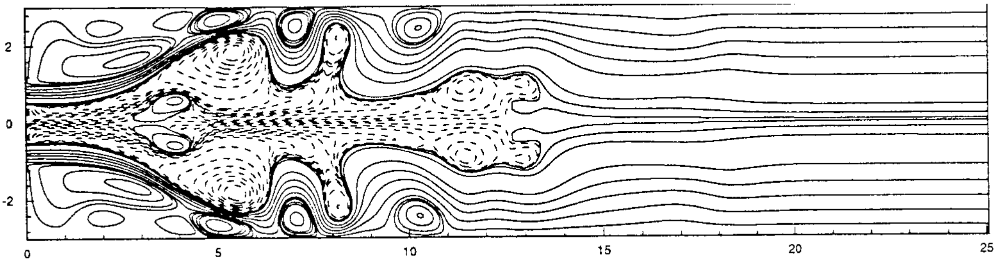

(h) t=96.83

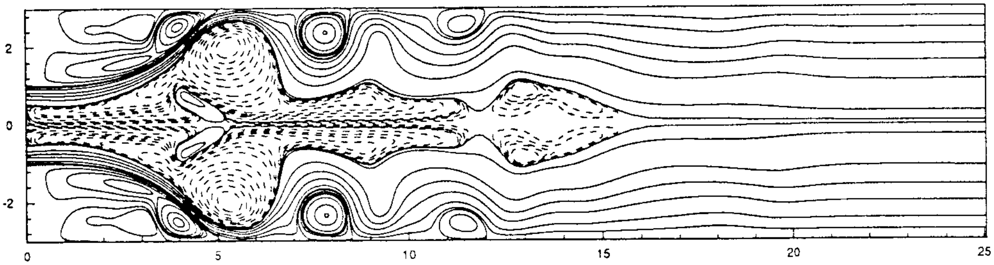

(i) t=107.59

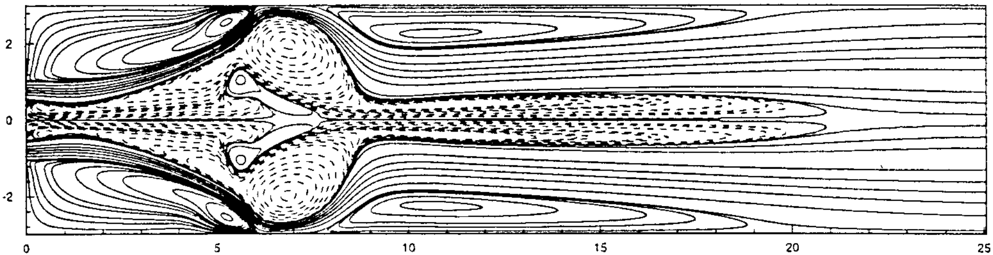

(j) t=497.85
(steady state)

Figure 9 (*Continued*)

annular flow causes the vortex shedding from the central recirculation bubble to disappear when the flow is in the transition region. The central recirculation zone behind the center-body becomes stable when the flow regime changes from the transition to the penetration region. Moreover, the length of the central recirculation bubble is changed under the influence of the swirling flow. When S is increased to be larger than 0.1, the flow is in the penetration region, the fluid moves downstream in the central region of the recirculation bubble and passes through the reicrculation zone. The accumulated fluid in the bubble is carried outward, and this phenomenon results in the recirculation length becoming shorter as the swirl number is increased.

For the numerical simulation, a 128 × 512 grid system, with $\Delta r = 0.022$, $\Delta z = 0.045$, and the time step $\Delta t = 0.01$, is used for the computations. The initial conditions for these computations are chosen to be motionless fluid. The calculation begins with $Re = 630$ and $S = 0$. As the steady state solution is obtained, the swirl effect is added to the flow with an increment of the swirl number S being 0.05 in every computation. The results for the relationship between the length of the central recirculation bubble behind the center-body and the swirl number are depicted in Figure 12. The computational results are in good agreement with the experimental data.

Figure 13 gives a series of the transient flow structures for the flow with $Re = 630$ and $S = 0.25$. The flow pattern is called vortex breakdown. The initial condition for this computation is chosen to be the steady state solution for $Re = 630$ and $S = 0$. The swirl effect of

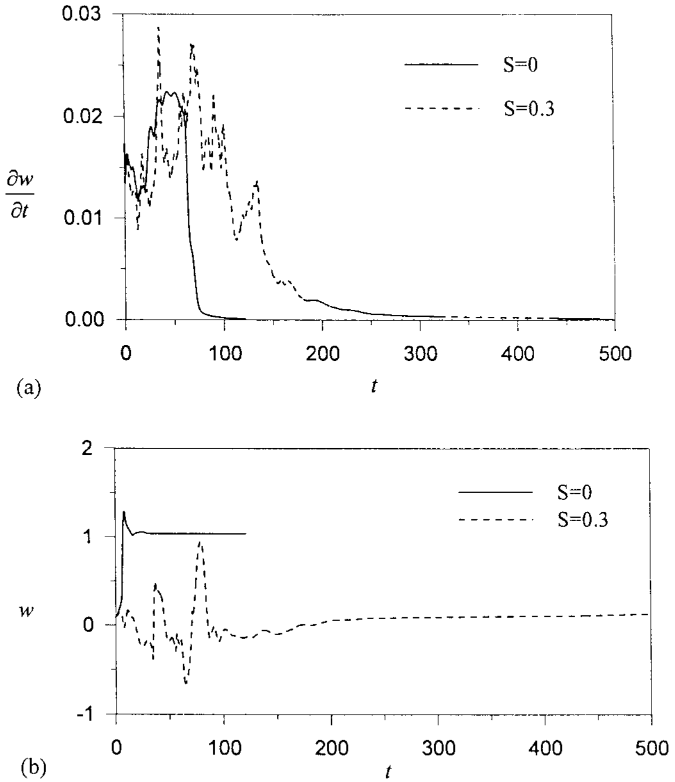

Figure 10. (a) Time history of the root mean square values of the acceleration $\partial w/\partial t$, (b) local velocity w at (0.75, 3.13) for $Re = 300$ and $S = 0$; $Re = 300$ and $S = 0.3$.

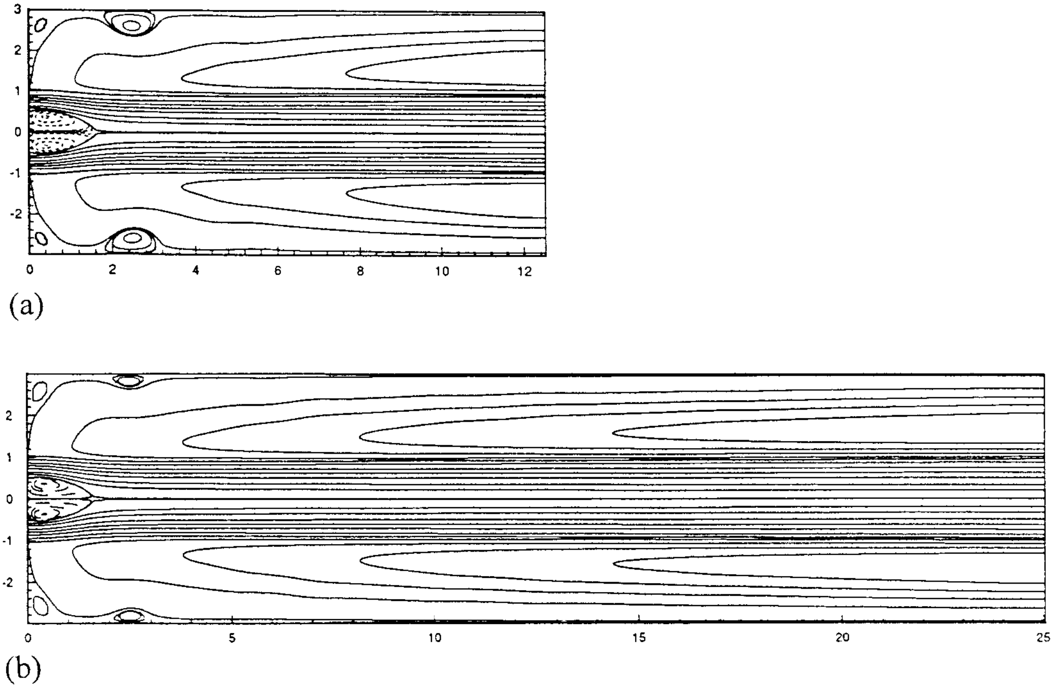

Figure 11. Comparison of the computational length for $Re = 630$ and $S = 0$; (a) $L = 6d_o$ (b) $L = 12d_o$.

$S = 0.25$ is then abruptly added into the inflow boundary condition. For the vortex-breakdown flow regime, an isolated recirculation zone appears downstream from the central recirculation zone when the swirl number reaches a critical value (e.g. $S = 0.18$ when $Re = 630$). Two pairs of vortex cells in the central recirculation zone can be observed (also see Figure 7). The secondary annular vortex with opposite vorticity is generated between the primary annular

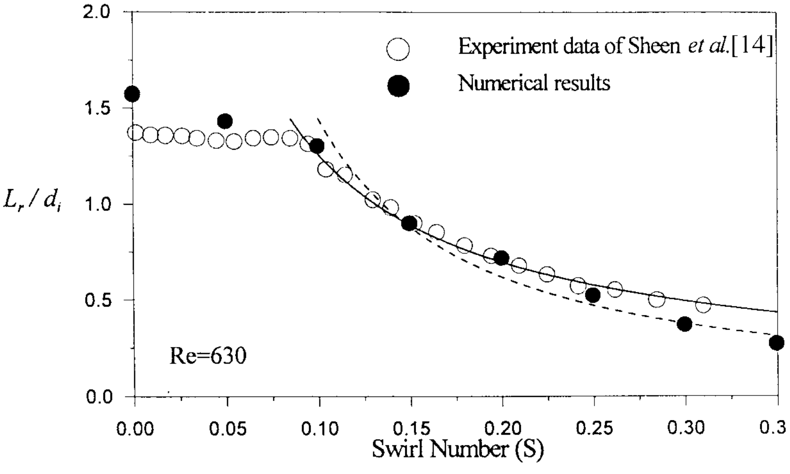

Figure 12. The relationship between the recirculation length behind the center-body and the swirl number S for $Re = 630$.

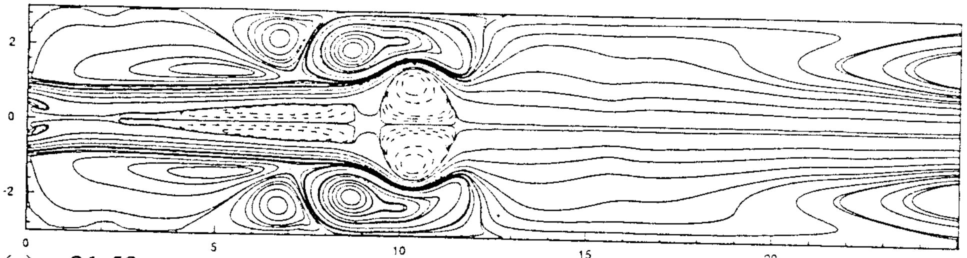

(a) t=21.52

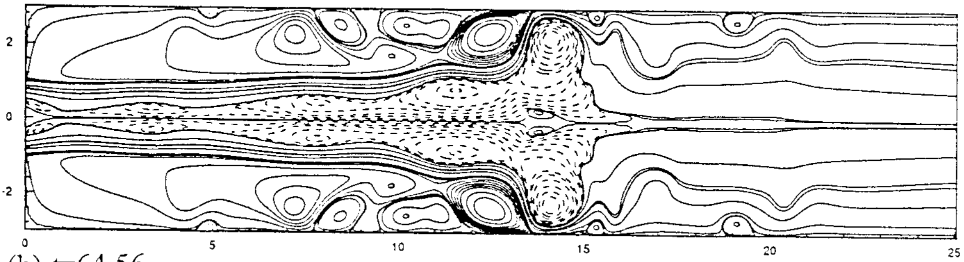

(b) t=64.56

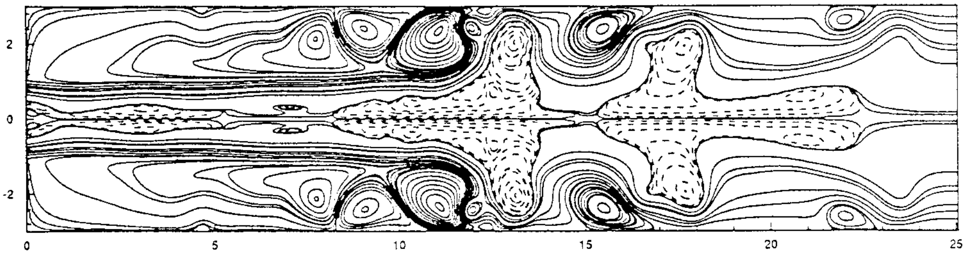

(c) t=107.59

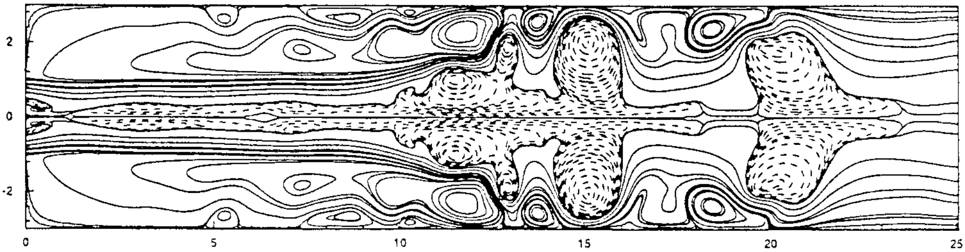

(d) t=150.64

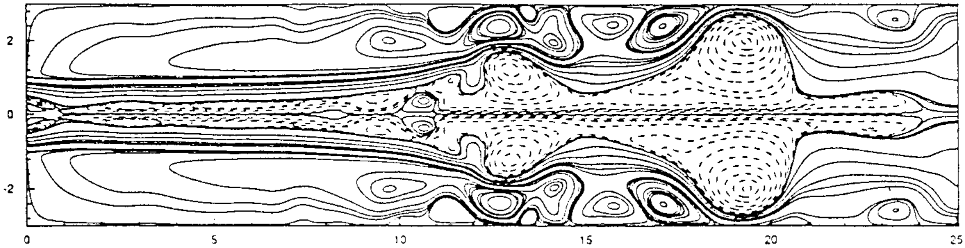

(e) t=215.2

Figure 13. The transient solutions of the flow structure in vortex-breakdown flow regime for $Re = 630$ and $S = 0.25$.

vortex and the base surface of the center-body. Furthermore, vortex breakdown occurs downstream. The stagnation point of the vortex breakdown moves upstream as the swirl number is increased. As shown in this figure, the flow structure becomes much more complicated. More computing time is needed to obtain the solutions. The size of the central recirculation zone decreases as the swirl number is increased. This phenomenon leads to a larger corner recirculation zone than in the attachment flow regime (see Figure 9).

4. CONCLUSIONS

A numerical simulation is proposed to investigate the flow structures of a confined annular swirling flow in the laminar flow regime. An explicit Adams–Bashforth scheme for momentum equations and the projection method are used to obtain the pressure Poisson equation so that the continuity equation can be satisfied automatically. The pressure Poisson equation is then solved directly by using the FFT and TDMA. For this study, the test section and the inflow boundary condition are taken from the experiments. As the linearized convective outflow boundary conditions are imposed, the required computational length in this numerical simulation is considerably reduced. Second-order-accurate solutions in both time and space discretizations can be obtained by this proposed numerical method. The most significant advantage of this numerical scheme is to avoid the time-consuming iteration processes for solving the pressure and the velocity fields. Therefore, a more efficient numerical scheme is obtained.

In this study, several flow cases are investigated. The computational results are in good agreement with the experimental data in general. Various flow patterns, based on the parameters of the Reynolds number and the swirl number, can be obtained by this numerical simulation, e.g. closed toroid, prepenetration, penetration, vortex breakdown, attachment. Furthermore, it is found that the flow structure of a swirling flow is more complex and unstable than that of a non-swirling flow. The central recirculation length increases with the Reynolds number for a non-swirling flow. The central recirculation zone remains comparatively small in the flow regimes other than the attachment regime. This result leads to a relatively large corner recirculation zone behind the expansion step. In the attachment flow regime, the central recirculation zone joins the isolated recirculation zone and results in a small corner recirculation zone. Moreover, the swirling motion has an effect on reducing the length of the central recirculation bubble.

It is clear that the flow structures of an annular swirling flow are very complex as indicated in the experiment of Sheen *et al.* [14] and in this numerical investigation. Further studies on the flow structures of other flow regimes by using a three-dimensional numerical model [20] and the transient process of the unsteady flow phenomenon are in progress.

ACKNOWLEDGMENTS

This research was supported by the National Science Council of Taiwan, under grant number NSC85-2211-E035-014.

APPENDIX A. NOMENCLATURE

d_h hydraulic diameter of the annulus, $d_\mathrm{h} = d_\mathrm{o} - d_\mathrm{i}$
d_i inner diameter of the annulus

d_o	outer diameter of the annulus
D_e	diameter of the confined pipe
L	length of the confined pipe
L_r	length of the central recirculation bubble
p	pressure
r	radial co-ordinate
Re	Reynolds number
S	swirl number
t	time
u	radial velocity
v	azimuthal velocity
$\bar{v}$	volumetric mean azimuthal velocity
w	axial velocity
$\bar{w}$	volumetric mean axial velocity
z	axial co-ordinate
ρ	density
ϕ	guide-vane angle
θ	azimuthal co-ordinate
ν	kinematic viscosity

REFERENCES

1. J.M. Beer and N.A. Chigier, *Combustion Aerodynamics*, Wiley, New York, 1972.
2. N. Syred and J.M. Beer, 'Combustion in swirling flows: a review', *Combust. Flame*, **23**, 143–201 (1974).
3. D.G. Lilly, 'Swirl flows in combustion: a review', *AIAA J.*, **15**, 1063–1078 (1977).
4. A.M.K.P. Taylor and J.H. Whitelaw, 'Velocity characteristics in the turbulent near wakes of confined axisymmetric bluff bodies', *J. Fluid Mech.*, **139**, 391–416 (1984).
5. X. Li and R.S. Tankin, 'A study of cold and combusting flow around bluff body combustors', *Combust. Sci. Tech.*, **52**, 173–206 (1987).
6. N.A. Chigier and J.M. Beer, 'Velocity and static pressure distributions in swirling air jets issuing from annular and divergent nozzles', *Trans. ASME J. Basic Eng.*, **86**, 788–796 (1964).
7. D.L. Rhode, D.G. Lilly and D.K. McLaughlin, 'Mean flow fields in axisymmetric combustor geometries with swirl', *AIAA J.*, **21**, 593–600 (1983).
8. M.P. Escudier and J.J. Keller, 'Recirculation in swirling flow: a manifestation of vortex breakdown', *AIAA J.*, **23**, 111–116 (1985).
9. J.K. Harvey, 'Some observations of the vortex breakdown phenomenon', *J. Fluid Mech.*, **14**, 585–592 (1962).
10. T. Sarpkaya, 'Vortex breakdown in swirling conical flows', *AIAA J.*, **9**, 1792–1799 (1971).
11. V. Shtern, A. Borissov and F. Hussain, 'Vortex sinks with axial flow: solution and applications', *Phys. Fluids*, **9**, 2941–2959 (1997).
12. H.J. Sheen, W.J. Chen, S.Y. Jeng and T.L. Huang, 'Correlation of swirl number for a radial-type swirl generator', *Exp. Therm. Fluid Sci.*, **12**, 444–451 (1996).
13. H.J. Sheen, W.J. Chen and J.S. Wu, 'Flow patterns for an annular flow over an axisymmetric sudden expansion', *J. Fluid Mech.*, **350**, 177–188 (1997).
14. H.J. Sheen, W.J. Chen and S.Y. Jeng, 'Recirculation zones of unconfined and confined annular swirling jets', *AIAA J.*, **34**, 572–579 (1996).
15. F. Nataf, 'An open boundary condition for the computation of the steady incompressible Navier–Stokes equations', *J. Comput. Phys.*, **85**, 104–129 (1989).
16. F.H. Harlow and J.E. Welch, 'Numerical calculation of time-dependent viscous incompressible flow of fluid with free surface', *Phys. Fluids*, **8**, 2182–2189 (1965).
17. A.J. Chorin, 'Numerical solution of Navier–Stokes equations', *Math. Comput.*, **22**, 745–762 (1968).
18. S.V. Patankar, *Numerical Heat Transfer and Fluid Flow*, Hemisphere, Washington DC, 1980.
19. D.L. Young and C.B. Liao, 'The Hopf bifurcation in the cylindrical cavity', *Numerical Methods in Laminar and Turbulent Flow*, vol. 7, Pineridge Press, Swansea, UK, 1991, pp. 729–739.
20. C.B. Liao and D.L. Young, 'A semi-implicit projection method for solving transient 3D flow in cylindrical co-ordinates system', *Proc. 2nd Asian Computational Fluid Dynamics Conference*, Tokyo, Japan, 1996, pp. 319–324.